Magnon Dynamics in Parity-Time-Symmetric Dipolarly Coupled Waveguides and Magnonic Crystals

Xi-guang Wang,[1,*] Dominik Schulz,[2] Guang-hua Guo,[1] and Jamal Berakdar[2]

[1] *School of Physics and Electronics, Central South University, Changsha 410083, China*

[2] *Institut für Physik, Martin-Luther Universität Halle-Wittenberg, 06099 Halle/Saale, Germany*

(Received 26 March 2022; revised 6 July 2022; accepted 2 August 2022; published 30 August 2022)

We consider the magnonic properties of two dipolarly coupled magnetic stripes, both deposited on a normal conductive substrate with strong spin-orbit coupling. A charge current in the substrate acts on the adjacent magnets with spin-orbit torques, which result in magnonic damping or antidamping of the spin waves, and hence a gain-loss coupling of the two magnetic stripes. The whole setup is demonstrated to exhibit features typical for parity-time- (*PT*) symmetric systems. Phenomena are demonstrated that can be functionalized in magnonic devices, including reconfigurable magnonic diodes and logic devices. Alternative stripe designs and *PT*-symmetric, periodic, coupled magnonic textures are studied. Analytical and full numerical analysis identify the conditions for the appearance of exceptional points (EPs), where magnonic gain and loss are balanced and evidence nonreciprocal magnon propagation and enhanced magnon excitation around EPs. Furthermore, the dipolar coupling is shown to bring in a wave-vector-dependent *PT*-symmetric behavior. Proposing and simulating a *PT*-symmetric magnonic crystal, we show how EPs and hence associated phenomena can be steered to a particular wave vector in a gaped spectrum via material design. The phenomena offer additional tools for magnonic based communication and computational devices.

DOI: 10.1103/PhysRevApplied.18.024080

I. INTRODUCTION

Magnons are the quanta of low-energy collective (spin-wave, SW) excitations in a magnetically ordered material. Magnonic devices utilize SW signals to transfer and/or process information at a relatively low-energy cost, high operation frequency, and without Joule heating [1–3]. Proposals and realizations of such devices include, for example, magnonic logic gates, phase shifters, and magnon transistors [4–11]. A good magnonic device performance goes along with efficient and versatile control of the magnon propagation in the SW channels. In this context, coupled magnonic waveguides (WGs) are essential building blocks as they allow steering and transmitting the SW signals to various units in a magnonic circuit [12–19]. A key enabling feature is the magnetic coupling between the waveguides, which renders possible the operation of magnonic directional coupler, power splitter, multiplexer, half-adder, and others [12–19]. External tools to trigger and act on the SW signal include magnetic and electric fields, or spin-transfer and spin-orbit torques. On the other hand, the limiting factors for applications include the relatively long response time of magnetic dynamics, the necessity for a strong magnetoelectric coupling or large charge-current densities if electric fields are to be used. Thus, alternative design proposals are helpful and can shed light on different physical aspects of coupled SW excitations.

In recent years, non-Hermitian *PT*-symmetric systems have been discussed in quantum mechanics [20–22], optics [23–27], acoustics [28,29], electronics [30,31], and magnonics [32–40]. For such systems, it is possible to achieve an exceptional point (EP) where the *PT*-symmetry phase breaking occurs [23–25,27,38]. Near the EP, the *PT*-symmetric systems possess several unusual properties, which are widely discussed for various promising applications [41–45]. For example, by introducing balanced gain and loss in coupled magnetic layers, magnonic *PT* symmetry was generated. Gain (loss) here means antidamping (damping) of magnonic excitations. Varying the ratio between gain and loss, the coupled magnonic system can be tuned to the *PT*-symmetry broken phase at the EP, where two or more magnon eigenmodes coalesce simultaneously. In this process, the orthogonality between different eigenmodes is gradually weakened, leading to a nonreciprocal magnon propagation. Injecting magnons in different magnetic layers, the magnon profile is then not reciprocally switched [37]. In the vicinity of the EP, the magnon excitation efficiency and the response to external disturbance are substantially enhanced [37,38,46]. Above the EP, an abrupt spin reversal is observed. Besides, by varying appropriately some external parameters (such

*wangxiguang@csu.edu.cn

 © 2022 American Physical Society

as the magnetic field) we can encircle the EP and so switch freely between different magnon eigenmodes [38]. Such features are interesting for applications in magnonic logics, more sensitive sensors for external magnetic changes, magnonic amplifiers, or applications to magnetic switching. Recent studies concentrate on the coupling between the magnetic waveguides via the interlayer exchange (Ruderman-Kittel-Kasuya-Yosida, RKKY) interaction. Even though RKKY-coupled magnetic layers are experimentally feasible, the RKKY coupling is strongly sensitive to interface properties and requires (for our purpose) a high degree of control on the quality and thickness of the spacer layer.

A more general and versatile setup is offered by dipolarly coupled waveguides whose utility for magnonics has already been demonstrated [12,14]. Here we propose and study the theoretical aspects of *PT*-symmetric dipolarly coupled waveguides. Using a combination of micromagnetic simulations and analytical theory, we present designs where two dipolarly coupled WGs deposited on the normal (heavy) metal show a *PT*-typical behavior when driving a current density in the substrate. Contrasting with the RKKY case, the dipolar coupling strength is weaker, with the result that a relatively small electric current density is sufficient to drive the system between the *PT*-symmetry preserving and broken phases across the EP. In addition, for the dipolarly coupled WGs, we find a wave-vector-dependent *PT*-symmetric behavior. In some ranges, where the dipolarly coupled magnon modes are degenerate, the electric current density at EP can approach zero. Varying the distance between the two WGs periodically, magnonic bands are formed [47,48]. By driving the system to the vicinity of the EP, the magnonic amplitude is strongly enhanced at the Brillouin-zone (BZ) boundary. This opens the possibility for having a gaped spectrum with a wave-vector-specific magnon-amplitude enhancement and increased sensitivity by adjusting the structuring period.

II. ANTIPARALLEL ALIGNED MAGNETIC STRIPES

The proposed structure is shown in Fig. 1(a). The magnons are excited and propagate in two dipolarly coupled waveguides, WG1 and WG2. For triggering the magnons and manipulating the magnonic *PT* symmetry, local magnetic fields, the substrate electric currents, and the interfacial spin Hall effects are exploited. The latter leads to the spin-orbit torque (SOT) $\mathbf{T}_p = \gamma c_J \mathbf{m}_p \times \hat{\mathbf{x}} \times \mathbf{m}_p$ acting on the layer $p = 1, 2$ with the magnetization unit vector field $\mathbf{m}_p$. SOT strength is given by c_J (with a sign dependent on the charge-current direction), and γ is the gyromagnetic ratio. If the magnetizations in the two WGs are opposite, the SOT results in losses and gains in the amplitudes of the dipolarly coupled magnonic modes.

Generally, the dipolarly coupled magnetization dynamics is governed by the Landau-Lifshitz-Gilbert

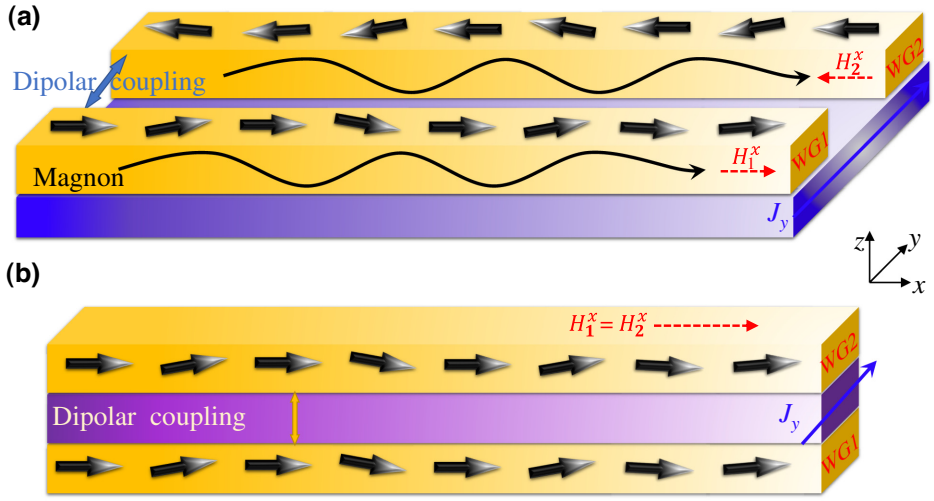

FIG. 1. (a) Schematics of two dipolarly coupled magnonic waveguides WG1 and WG2 (magnetized oppositely along the x axis) and deposited on a heavy-metal substrate (for example Pt). The magnons are launched locally at the left end ($x = 0$) in WG1 or WG2. Injecting in the Pt layer a charge current J_y results in spin-orbit torques (SOTs) acting on both magnetic layers but with opposite directions. Therefore, the SOT damp or antidamp the magnons in WG1 or WG2 allowing so to realize a *PT*-symmetric system with the magnon propagation having particular features controllable by SOTs (or J_y). The static fields H_1^x and H_2^x in WG1 and WG2 have equal magnitude and opposite directions. Such fields can be realized by attaching separated bias layers to the waveguides. (b) Schematic of two dipolarly coupled magnonic waveguides WG1 and WG2 (magnetized along the x axis). Injecting in the spacer Pt layer a charge current J_{Pt} acts with opposite SOTs on WG1 and WG2, meaning it damps one waveguide and antidamps the other. In this way, the *PT*-symmetry phases, and correspondingly the inherent feature of the magnon propagation, can be controlled.

(LLG) equations [49,50],

$$\frac{\partial \mathbf{m}_p}{\partial t} = -\gamma\, \mathbf{m}_p \times \mathbf{H}_{\text{eff},p} + \alpha\, \mathbf{m}_p \times \frac{\partial \mathbf{m}_p}{\partial t} + \mathbf{T}_p. \quad (1)$$

M_S is the local saturation magnetization. μ_0 is the vacuum permeability, and α is the intrinsic Gilbert damping in the respective layer. The effective field $\mathbf{H}_{\text{eff},p} = (2A_{\text{ex}}/\mu_0 M_S)\nabla^2 \mathbf{m}_p + H_p^x \hat{\mathbf{x}} + \mathbf{H}_{\text{demag}}$ consists of the internal exchange field (with an exchange constant A_{ex}), the external magnetic field H_p^x, and the demagnetization field. The magnetic dipole-dipole interactions are included in the demagnetization field:

$$\mathbf{H}_{\text{demag}}(\mathbf{r}) = -\frac{M_S}{4\pi}\nabla \int_{V'} \nabla' \frac{1}{|\mathbf{r} - \mathbf{r'}|} \cdot \mathbf{m}(\mathbf{r'}) dV'. \quad (2)$$

We study the magnon dynamics by using linearized analytical models, supported and complemented with numerical simulations of Eq. (1) that allow assessing the validity of the linear regime.

The predictions are generic (also when including spin-transfer torques for conductive ferromagnets) for the sake of demonstration, we perform the simulations for magnetic layers made of yttrium iron garnet [$Y_3Fe_2(FeO_4)_3$, YIG] corresponding to $M_S = 1.4 \times 10^5$ A/m, $A_{\text{ex}} = 3 \times 10^{-12}$ J/m, and Gilbert damping $\alpha = 0.001$. The magnetic field along the axis of the waveguide (x axis) is $H_1^x = -H_2^x = 10$ mT. The small bias field H_p^x can be generated via coupling fields from attaching bias layers. The two stripes have the same extensions with a width of $w = 100$ nm (along y axis), thickness $h = 50$ nm (along z axis). The space between the WGs is $\delta = 100$ nm wide.

To launch the magnons, we start from the initially antiparallel magnetization [$\mathbf{m}_1 = (1, 0, 0)$ and $\mathbf{m}_2 = (-1, 0, 0)$] and relax to the stationary state. A periodic magnetic field pulse $h(t) = h_a \mathbf{z} \sin(2\pi f_H t)/(2\pi f_H t)$ is then applied locally to WG1 at $x = 0$, which results in propagating magnons over a wide frequency range. Here, the excitation cutoff frequency is $f_H = 25$ GHz, and the field amplitude is $h_a = 25$ mT. In the simulations, we analyze the magnetization fluctuations extracted from each cell M_z during 200 ns with a time step of 20 ps. To obtain the magnon dispersion relation, we use a two-dimensional fast Fourier transform $M_z(k_x, f) = (1/N)\sum_{q=1}^{N_y} F_2[M_z(x, y_q, t)]$, where y_q is the qth cell along the y axis, where N_y is the total number of cells along the y axis. The cell size adopted in the simulation is $20 \times 20 \times 50$ nm^3. In the coupled waveguides with strong shape anisotropy, the parallel or antiparallel configurations are both stable. To realize the initial antiparallel magnetizations, at first we drive the system to a state of parallel magnetizations in two magnetic layers using a high magnetic field (much larger than the amplitude of the small bias field H_p^x). Then, a short perpendicular magnetic field pulse triggers the flip between the parallel and antiparallel states [12,51,52].

The numerical magnon dispersion relation obtained for two dipolarly coupled waveguides is shown in Fig. 2(a). The dispersion curves exhibit similar features with backward volume SW modes, with the group velocity being negative in the low wave-vector range ($|k_x| < 0.015$ nm^{-1}), and the exchange term dominates the dipolar term in the larger k_x range. The dipolar coupling between WG1 and WG2 leads to the formation of lower "acoustic" and higher "optic" modes. Due to the nature of dipolar coupling, in the low-frequency range with large wavelength, the difference between the two magnon modes is more obvious, and declines with increasing frequency f. At a certain f, the two magnon modes with different wave vectors are excited simultaneously, and their interference leads to a periodic transfer of magnonic power between the WGs, as demonstrated by Fig. 2(b). The coupling length is larger for larger frequencies, where the wave-vector difference between the two modes is smaller, see the left column of Figs. 2(a)–2(c). Furthermore, the splitting between the two SW modes decreases with the spacing thickness between the two WGs as the dipolar coupling strength increases while the spacing thickness shrinks.

For an analytical insight we assume the magnetization vectors to deviate slightly from their equilibrium states (long-wavelength SW limit), meaning $\mathbf{m}_p(\mathbf{r}, t) = \mathbf{m}_{0,p} + \mathbf{m}_{s,p} e^{i(\mathbf{k}_s \cdot \mathbf{r} - \omega t)}$. Here, $\mathbf{m}_{0,1} = -\mathbf{m}_{0,2} = \hat{\mathbf{x}}$ is the static antiparallel equilibrium magnetization, and the small deviation from equilibrium is $\mathbf{m}_{s,p} = (0, \delta m_{y,p}, \delta m_{z,p})$ with $\delta m_{y(z),p} \ll 1$. The wave vector $\mathbf{k}_s$ is the sum of the in-plane wave vectors $\mathbf{k} = k_x \hat{\mathbf{x}} + k_y \hat{\mathbf{y}}$. In Fourier space, the linearized LLG equation with SOT yields the following expression for the SWs [12,37,53]:

$$-i\omega \mathbf{m}_{s,p} = \mathbf{m}_{0,p} \times \sum_q \hat{\Omega}_{pq} \cdot m_{s,q} - \mathbf{m}_{0,p} \times (i\alpha\omega \mathbf{m}_{s,p} - \omega_J \hat{\mathbf{x}} \times \mathbf{m}_{s,p}). \quad (3)$$

Here, $\omega_J = \gamma c_J$, and the tensor $\hat{\Omega}_{pq}$ has the form

$$\hat{\Omega}_{pq} = \Omega_0 \delta_{pq} \hat{I} + \omega_{\text{M}} \hat{F}(d_{|p-q|}). \quad (4)$$

We define $\Omega_0 = \gamma H_1^x + 2\gamma A_{\text{ex}} k^2/\mu_0 M_S$, and $\omega_M = \gamma M_S$. The wave vector k is equal to $\sqrt{k_x^2 + k_y^2}$, the distance between the two consecutive WGs is $d_1 = w + \delta$. The dynamic magnetodipolar interaction is described by the tensor $\hat{\mathbf{F}}$:

$$\hat{\mathbf{F}}(d_p) = \int \hat{\mathbf{N}}_k e^{ik_y d_p} \frac{dk_y}{2\pi}, \qquad \hat{N}_k^{\alpha\beta} = \frac{\sigma_s^2(k_y)}{w_s} \int D_p(k_z) D_q^*(k_z) \frac{k_\alpha k_\beta}{k^2} \frac{dk_z}{2\pi}. \quad (5)$$

The "shape amplitude" $D_p(k_z) = \int_{-h/2}^{h/2} e^{-ik_z z} dz = h\,\text{sinc}(hk_z/2)$ describes the influence of the finite thickness h of

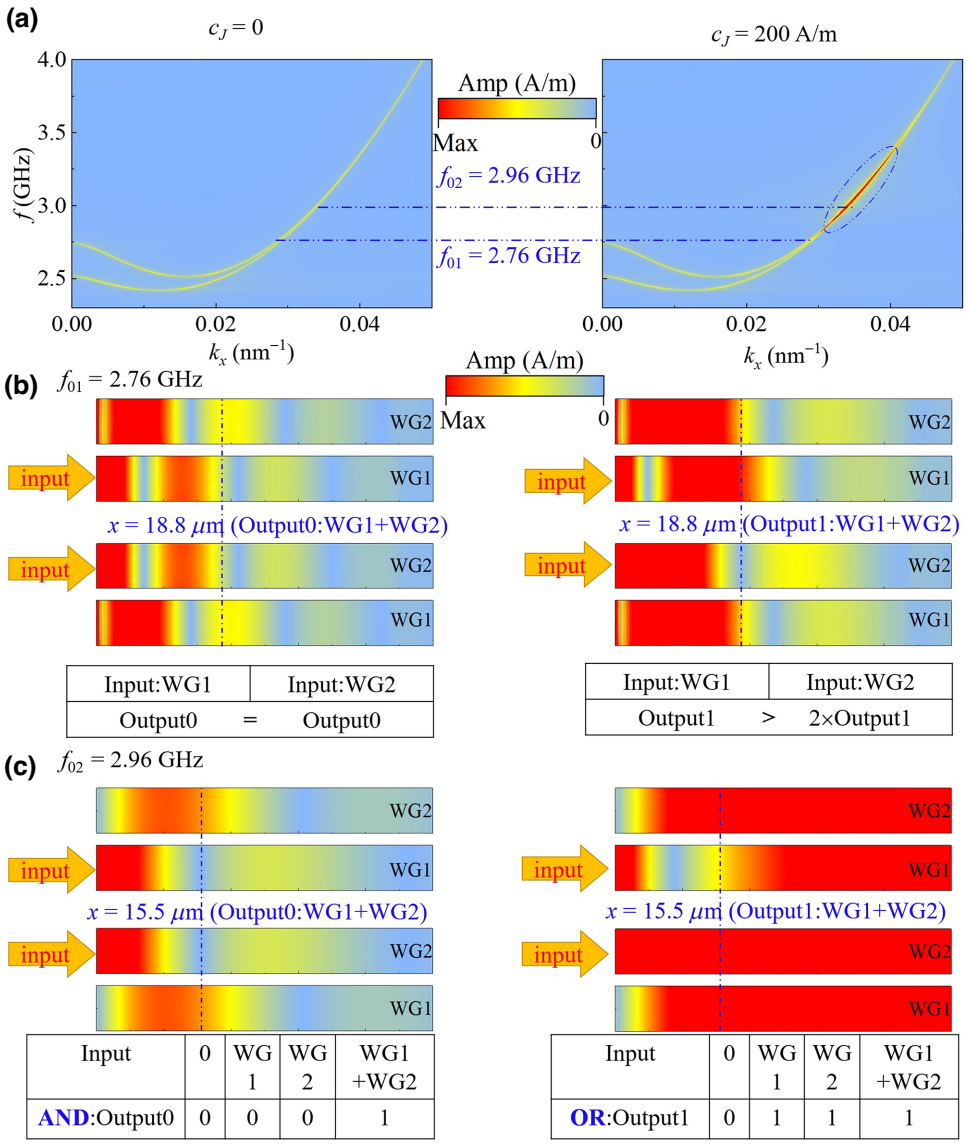

FIG. 2. (a) Simulated SW dispersion curves (frequency f versus wave vector k_x) of the magnons (showing the optic and acoustic modes) of the dipolarly coupled waveguides. At the frequency (b) $f = 2.76$ GHz and (c) $f = 2.96$ GHz, the spatial profiles of the magnon amplitudes in WG1 and WG2. The injected SWs are excited at $x = 0$ in WG1 (i.e., Input:WG1) or WG2 (i.e., Input:WG2). The outputs are detected via the sum of SW amplitudes in WG1 and WG2 at (b) $x = 18.8$ μm or (c) $x = 15.5$ μm. Here, left and right columns are for $c_J = 0$ and $c_J = 200$ A/m, respectively.

the thin WG. Here, $\sigma_s = \int_{-w/2}^{w/2} m(y) e^{-ik_y y} dy$ is the Fourier transform of the SW profile $m(y)$ across the width direction, and the effective width $w_s = \int_{-w/2}^{w/2} m^2(y) dy$. For a narrow WG we may assume $m(y) \sim \cos(\kappa y)$ for $\kappa = 0$, in which case the effective width is equal to the WG width and $\sigma_s = w\,\mathrm{sinc}(wk_y/2)$. Introducing $\psi_p^{\pm} = \delta m_{y,p} \pm i\delta m_{z,p}$, we obtain the determining equation $\omega\boldsymbol{\psi} = \hat{H}\boldsymbol{\psi}$ for the eigenmodes $\boldsymbol{\psi} = (\psi_1^+, \psi_1^-, \psi_2^+, \psi_2^-)$ at the SW eigenfrequencies ω. Inspecting Eq. (3), we infer the structure of the 4×4 operator $\hat{H}$ as

$$\hat{H} = \begin{pmatrix} -\tilde{\omega}^- - i\omega_J^- & \Delta\omega_0^- & -\bar{\omega}_1^- & \Delta\omega_1^- \\ -\Delta\omega_0^+ & \tilde{\omega}^+ - i\omega_J^+ & -\Delta\omega_1^+ & \bar{\omega}_1^+ \\ \bar{\omega}_1^+ & -\Delta\omega_1^+ & \tilde{\omega}^+ + i\omega_J^+ & -\Delta\omega_0^+ \\ \Delta\omega_1^- & -\bar{\omega}_1^- & \Delta\omega_0^- & -\tilde{\omega}^- + i\omega_J^- \end{pmatrix}. \tag{6}$$

We introduce the abbreviation $a/(1 \pm i\alpha) \equiv a^{\pm}$ for arbitrary a, and $\Delta\omega_j = \omega_j^z - \omega_j^y$ is the difference of the demagnetizing field for the y and z component, $\bar{\omega}_j = \omega_j^y + \omega_j^z$ is the sum of the demagnetizing field for the y and z component, and $\tilde{\omega} = \Omega_0 + \bar{\omega}_0$, where $\omega_j^y = (\gamma M_S/2)F^{yy}(d_j)$ and $\omega_j^z = (\gamma M_S/2)F^{zz}(d_j)$. $d_1 = w + \delta$ is the distance between WG1 and WG2. The waveguide interacting with its own dynamic demagnetizing field is captured for $j = 0$ ($d_0 = 0$).

Without SOT ($\omega_J = 0$), we obtain four eigenfrequencies ω for $\hat{H}$. Two positive frequencies correspond to right-handed precessions around the stable state, while the other two negative frequencies are associated with left-handed precessions. Applying a finite SOT with $c_J = 200$ A/m, the real parts of the two magnon modes turn identical for larger k_x [Figs. 3(a) and 3(b)], and the two imaginary parts are obviously separated [see Figs. 3(c) and 3(d)]. Considering the dependence of the eigenfrequencies on c_J

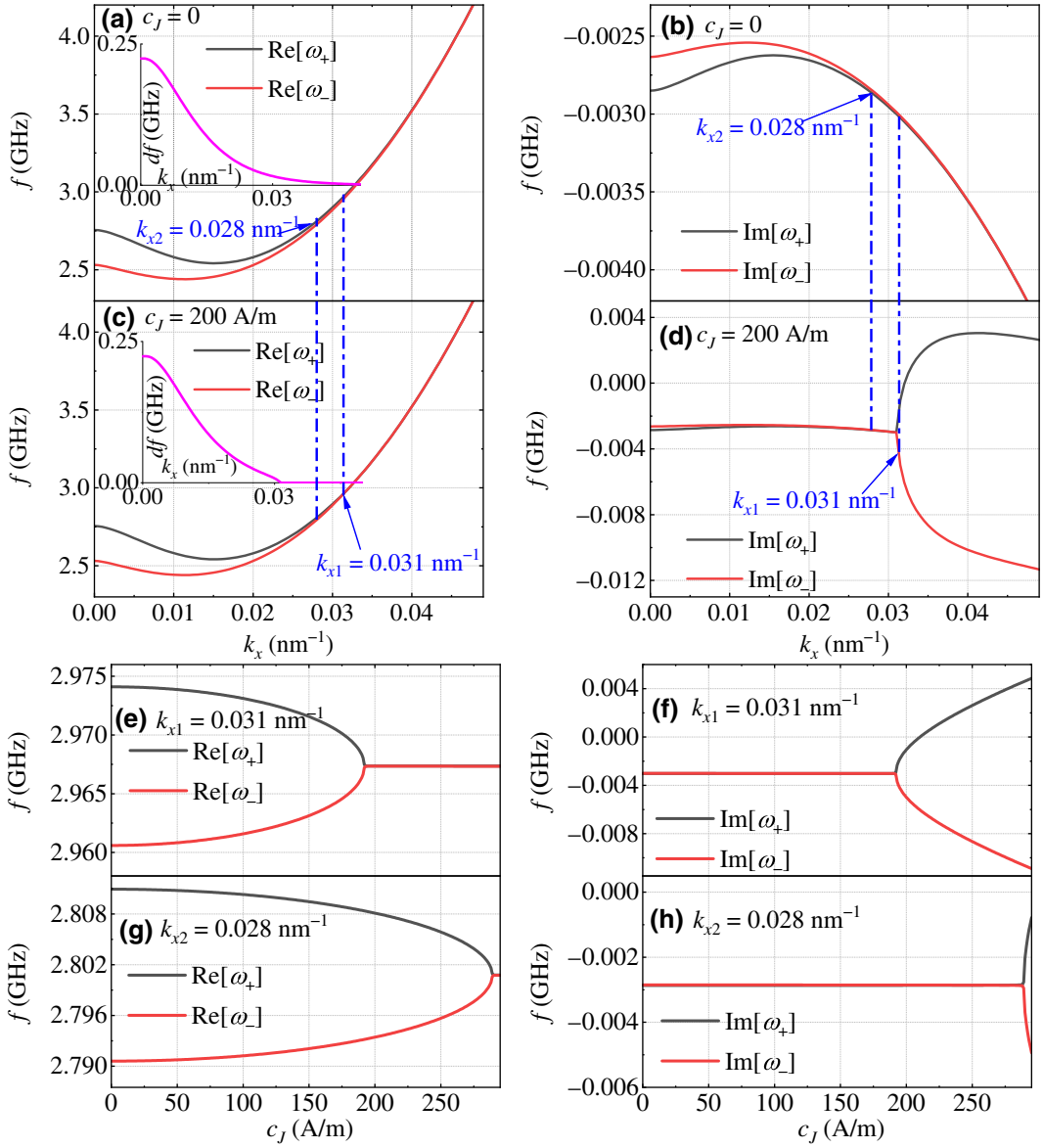

FIG. 3. (a)–(d) The analytical linearized model yields the real (dispersion) and the imaginary parts of two magnon eigenfrequencies $f = \omega/(2\pi)$ in the dipolarly coupled waveguides. Eigenfrequencies are obtained from the two positive eigenvalues of the matrix given by Eq. (6). The results are shown for $c_J = 0$ (a),(b) and $c_J = 200$ A/m (c),(d). The insets in (a)–(c) show $df = \mathrm{Re}[\omega_+ - \omega_-]/(2\pi)$. (e)–(h) Results of the analytical model for the real and the imaginary parts of the two magnon eigenfrequencies $f = \omega/(2\pi)$, as we scan c_J at the wave vector $k_x = 0.031$ and 0.028 nm^{-1}.

at different k_x [Figs. 3(e)–3(h)], for very small c_J the optical and the acoustic modes are still separated, and the two modes merge at a point (identified as the EP) when increasing c_J. Beyond the EP, the real parts of the two modes collapse at the same value and the imaginary parts bifurcate. This is a scenario known for EP in *PT*-symmetric systems. An interesting feature here is that the amplitude of c_J at the EP is dependent on k_x. For smaller k_x, the value of c_J for the occurrence of EP is larger. This explains why the two imaginary parts bifurcate at higher k_x for $c_J = 200$ A/m in Figs. 3(c)–3(d), as the magnons for low k_x are still below the EP, while they have surpassed the EP for higher k_x. Despite the relative simplicity and approximations, the analytical results agree well with those of micromagnetic simulations in Figs. 2(a) and 2(b). As well, in the simulations, the SW excitation is strongly enhanced at higher k_x when $c_J = 200$ A/m, which is in line with the altered imaginary parts in the analytical results in this regime. But there is still a slight quantitative difference between the simulations and the analytical results

due to the approximations made. For example, when $c_J = 200$ A/m there is a slight difference in the k_x range beyond the EP.

The changes in the two magnon modes affect the interference and the energy transfer between the WGs, as evidenced by the simulation results in Figs. 2(b)–2(c). For $c_J = 0$, meaning the conventional case, at a certain frequency, the superposition of the two modes (symmetric and antisymmetric) leads to a magnon periodic transfer between WG1 and WG2. The periodic transfer length L is directly related to the wave-vector difference between the two modes $L = \pi/|k_{x,+} - k_{x,-}|$ [12]. For a larger frequency, a smaller $|k_{x,+} - k_{x,-}|$ leads to a larger transfer length [Figs. 2(b)–2(c) when $c_J = 0$]. Besides, by changing from the antiparallel magnetization orientation to the parallel orientation, the coupling strength and $|k_{x,+} - k_{x,-}|$ become weaker and smaller (not shown), resulting in a larger transfer length L of the output power. Here, the magnon propagation is reciprocal. For example, in the left column of Figs. 2(b)–2(c), when switching the excitation from WG1 to WG2, the SW profiles in the two waveguides are also switched to each other.

When c_J is applied in the range below the EP [for example, $c_J = 200$ A/m and $f = 2.76$ GHz in Fig. 2(b)], in the unbroken *PT*-symmetric regime there are still two modes, but the two modes are not orthogonal anymore [25,37]. Thus, exchanging the input between WG1 and WG2 results in different SW profiles, i.e., the magnon propagation becomes nonreciprocal. Increasing the charge current c_J leads to a smaller $|k_{x,+} - k_{x,-}|$, meaning a larger transfer length L. For the case above the EP [for example, $c_J = 200$ A/m and $f = 2.96$ GHz in Fig. 2(c)], two modes coalesce and the SW can simultaneously propagate in both WGs. Here, one can still find the nonreciprocal feature, where the WG2 with gain always has a larger SW amplitude when the input is exchanged.

The nonreciprocal propagation in the electric current-induced *PT*-symmetric system points to potential applications in reconfigurable diode and logic devices. In Fig. 2(b) with frequency $f = 2.76$ GHz, when $c_J = 0$ two equal outputs are obtained by switching the input (SW injection) between WG1 and WG2 at $f = 2.76$ GHz. Turning on the electric current ($c_J = 200$ A/m), the SW output for "Input:WG1" becomes twice the out of "Input:WG2". Such a nonreciprocal result clearly points to a realization of a reconfigurable SW diode. The input in WG1 represents an "*on*" output with a larger amplitude, and input in WG2 signals an "*off* " state with an obviously smaller amplitude. Considering Fig. 2(c) with frequency $f = 2.96$ GHz, when $c_J = 0$ and the excitation is in both WG1 and WG2, only the symmetric SW mode is excited and the periodic propagation is *off*, resulting in the output with larger amplitude (logic "1") twice the output (logic "0") from other inputs (only in WG1 or WG2). This feature indicates a logic "AND" operation. When $c_J = 200$ A/m, the excitation is enhanced in both guides and the periodic transfer is also *off* above the EP. Here, larger SW amplitudes are achieved for input in WG1, WG2, or both waveguides, i.e., a logic "OR" operation, indicating an electrically reconfigurable SW logic device operated via the enhanced SW propagation above the EP.

The above analyses are only for antiparallel WG1 and WG2. For parallel configuration, there is still splitting between the optic and acoustic modes. Compared with

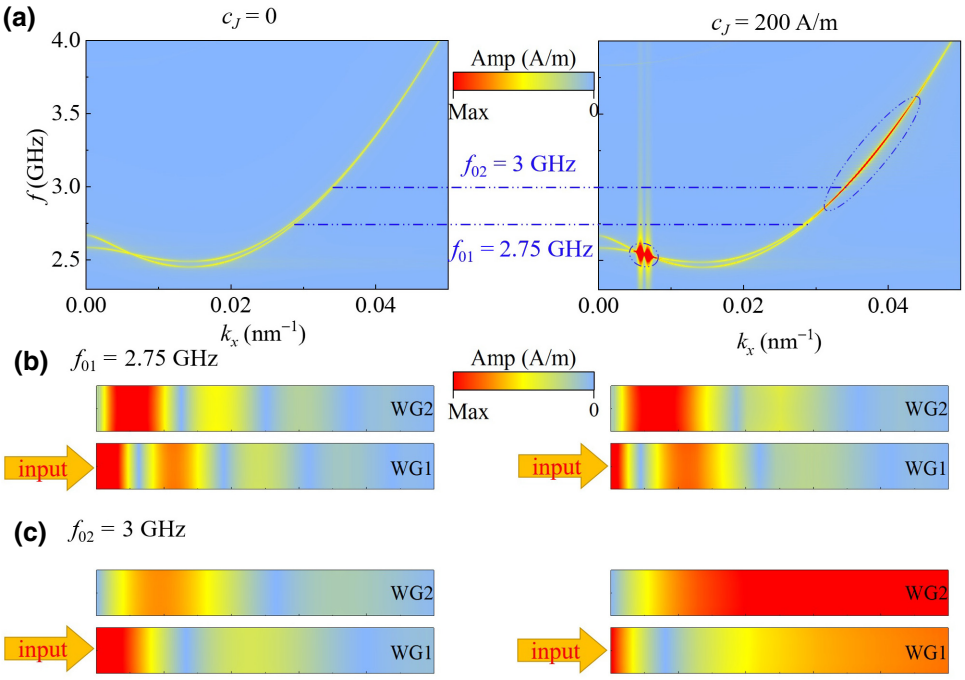

FIG. 4. Under the structure of Fig. 1(b), (a) the dispersion curves of two collective magnon modes (optic and acoustic modes) of coupled waveguides. (b),(c) The simulated spatial profiles of the propagating SW amplitude at (b) $f = 2.75$ GHz and (c) $f = 3$ GHz. Here, the SWs are excited at $x = 0$ in WG1, and left and right columns are for $c_J = 0$ and $c_J = 200$ A/m, respectively.

the antiparallel case, the mode splitting becomes slightly smaller under parallel configuration (not shown). Applying SOT on the parallel case can enhance or weaken the damping of coupled modes, and in such cases, one cannot achieve the *PT*-symmetry-phase change and EP. To realize the above effect in parallel waveguides, we provide a structure of Fig. 1(b), as discussed in the following section.

III. WAVEGUIDES WITH PARALLEL MAGNETIZATIONS

It is also possible to realize dipolarly coupled, *PT*-symmetric WGs with parallel magnetizations, as illustrated in Fig. 1(b). The spacer-induced SOT reads $\mathbf{T}_p = (-1)^p \gamma c_J \mathbf{m}_p \times \hat{\mathbf{x}} \times \mathbf{m}_p$. The simulation results for the dispersion relation are shown in Fig. 4(a) for a structure with a width $w = 100$ nm (along the y axis), thickness $h = 50$ nm (along the z axis), and a spacer thickness of $\delta = 100$ nm. The dispersion curves divert when the two modes cross at the low-frequency range [Fig. 4(a)]. For larger frequencies, the curves are similar to Fig. 2(a). The interference-induced power transfer between WG1 and WG2 is obvious at $f = 2.75$ GHz [Fig. 4(b)].

Following similar derivation steps, an analytical analysis is performed. The SW dispersion relation is presented in Fig. 5. For $c_J = 200$ A/m, the real parts and the imaginary

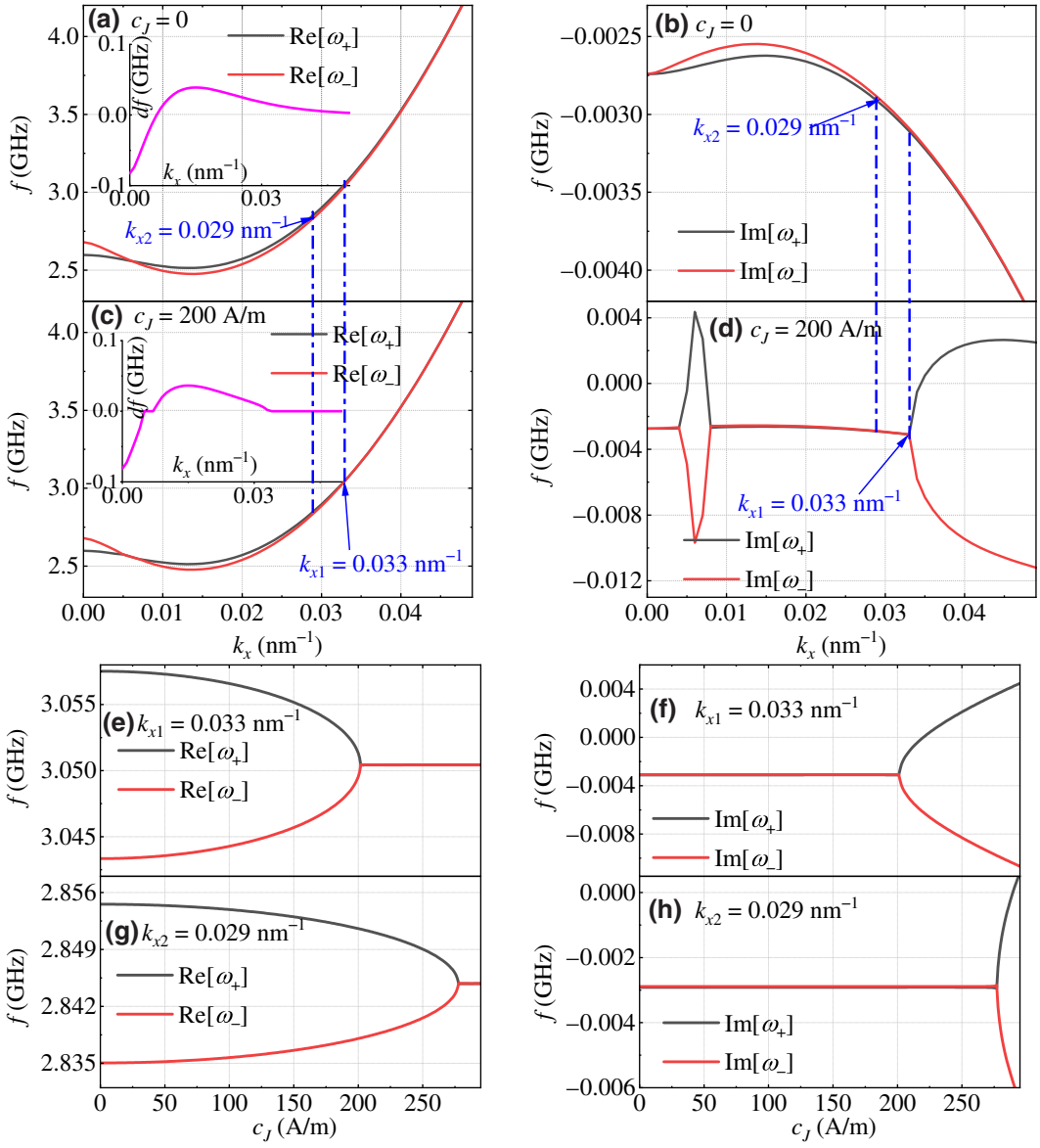

FIG. 5. For the structure of Fig. 1(b), numerically solving the analytical model delivers the real (dispersion) and the imaginary parts of the two magnon eigenfrequencies $f = \omega/(2\pi)$ in the dipolarly coupled waveguides for $c_J = 0$ (a),(b) and $c_J = 200$ A/m (c),(d). Here, the eigenfrequencies are obtained by the two positive eigenvalues of the magnon Hamiltonian [similar to Eq. (6)]. The insets in (a),(c) show $df = \mathrm{Re}[\omega_+ - \omega_-]/(2\pi)$. (e)–(h) Real and imaginary parts of two magnon eigenfrequencies $f = \omega/(2\pi)$ as we scan c_J at the wave vector $k_x = 0.033$ and 0.029 nm^{-1}.

parts are shown in Figs. 5(c)–5(d). Still, we observe that the real parts collapse and the imaginary parts bifurcate at higher k_x. In contrast, for lower k_x, the two modes cross even without SOT ($c_J = 0$). For $c_J = 200$ A/m the range with identical real parts of frequencies is enlarged, and in this range the imaginary parts are strongly separated. We note the cross modes decrease the required current density of EP to be around 0, thus reaching a value smaller than the current density needed for the auto-oscillation. Furthermore, by scanning c_J, we still find a k_x dependence of the EP, as evidenced by Fig. 5.

To endorse the above analysis, we simulate full numerically the SW propagation. As c_J approaches the EP, the change in the SW beating is shown by Fig. 4. A change in the imaginary parts at larger k_x and near the crossing point is evidenced by the SW excitation in the right column of Fig. 4(a), where the SW amplitude is strongly enhanced in the range above EP. Increasing the number of WGs does not alter qualitatively the features discussed above. An example of four WGs and some physical P and T operators [54] are presented in the Supplemental Material [55].

IV. *PT*-SYMMETRIC MAGNONIC CRYSTAL

In the preceding sections, our results demonstrate a feasible way for the realization of bridging the PT-symmetry phases when the two modes approach each other. In a magnonic crystal, the SW dispersion relation is folded at the Brillouin-zone boundary, where different magnon modes are merged, providing an alternative solution to easily drive the broken PT-symmetry phase and manipulate the SW propagation. The relevance of having a gaped spectrum with controllable dispersion is well documented in various areas such as electronics, photonics, and magnonics [24,48,56–63]. In particular, the transport properties are intimately related to the dispersion characteristics of the underlying structure, and determine for an electronic system for example, whether we have a band insulator or a metal. Electronic correlation introduces nonlinearities and multiple scattering between the otherwise independent effective single particles. Likewise, we expect for a magnonic system that introducing PT symmetry would allow amplifying nonlinear effects at a particular point in the dispersion, which could be of relevance to control multimagnon scattering and generation in a certain area in the BZ. As a demonstration we consider the periodic magnetic structure [illustrated by Fig. 6(a)]. The distance between WG1 and WG2 varies periodically. We note that in principle, comb-type magnetic stripes have already been fabricated [64]. The periodic modulations are reflected in correspondingly spatial changes in the internal effective fields that act on the SW and so generate a magnonic crystal [2,65–68]. As shown in Fig. 6(b), the magnon band is folded at the BZ boundary ($k_x = 0.04$ nm^{-1}). A clear band gap is identified between 2 and 4 GHz, where the magnon cannot propagate. We note, that the band gap at the BZ boundary approaches 0 in our model, similar to other magnonic crystals under particular geometric or magnetic parameters [63,69]. Applying a charge-current density to the waveguides results, as above, in opposite SOTs of the two magnetic stripes. The whole structure constitutes a PT-symmetric magnonic crystal. From the preceding discussion we expect the PT-symmetry-induced changes to be most prominent when the coupled bands cross. Here, the crossing occurs at the BZ boundary, and the exciting magnon amplitude is strongly enhanced, as demonstrated by the red color in the dispersion curve [Fig. 6(c)]. Increasing c_J further amplifies the magnon excitation and finally leads to the magnetization reversal, as demonstrated by the time dependent m_x in Fig. 7 ($c_J = 350$ A/m). The

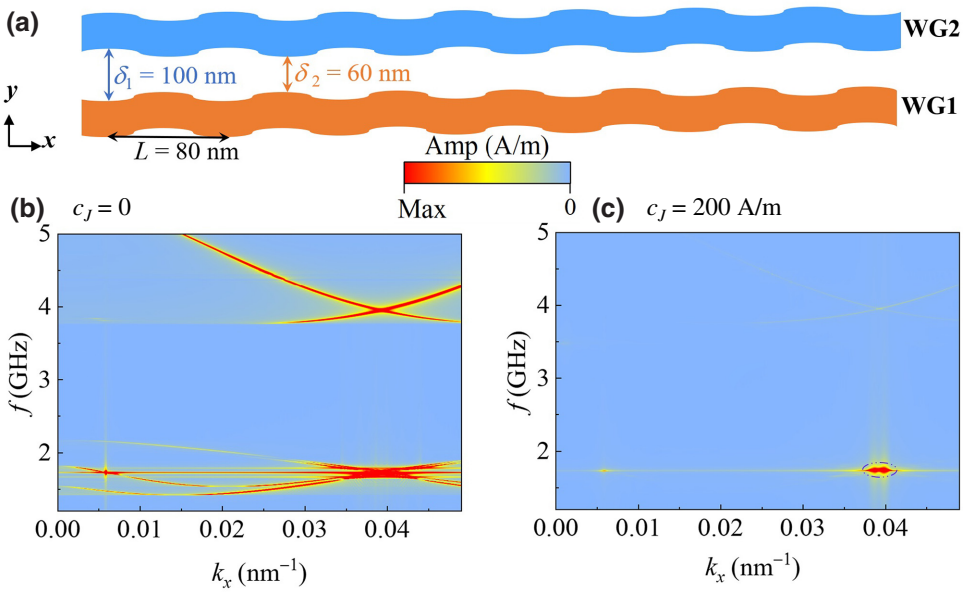

FIG. 6. (a) Schematic of periodic waveguides. The distance varies periodically between $\delta_1 = 100$ nm and $\delta_2 = 60$ nm, and period length $L = 80$ nm. For such a structure, the BZ boundary is at $k_x = \pi/L = 0.04$ nm^{-1}. (b),(c) Dispersion curves in the periodic waveguides for $c_J = 0$ (b) and $c_J = 200$ A/m (c).

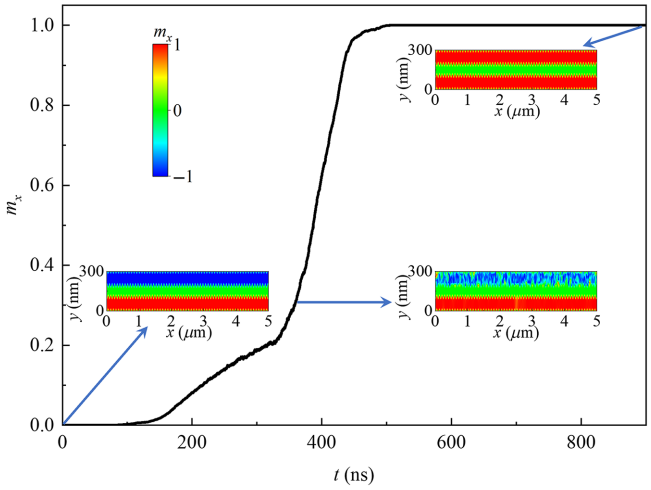

FIG. 7. Time dependence of total m_x of WG1 and WG2 for $c_J = 350$ A/m. Spatial profiles of m_x at different time points are shown as insets.

position of the wave-vector-dependent enhancement of the magnetic excitations is related to the spatial period of the modulations of the magnetic stripes and can be engineered desirably, thus allowing the study and use of nonlinear SWs at a controllable wave vector. As shown in Fig. 8, we shift the WG1 in $+x$ direction by 20 or 40 nm, the region with enhanced magnonic excitation is varied. For the displacement of 20 nm, a strongly localized magnon is excited near $f = 1.88$ GHz, causing the spectrum leakage (flat curve) in our calculation. As the Brillouin-zone boundary is controllable via the periodic parameter, one can use the electric current to selectively enhance the SW at the BZ boundary and control the emitting SW from the magnonic crystal structure via the above effect.

V. CONCLUSIONS

We present proposals for the designs of magnetic structures that serve for magnonic signal steering and amplification based on dipolarly coupled waveguides with a loss-gain mechanism induced by a charge current in a metallic substrate hosting a strong spin-orbit coupling. The magnonic signal can be steered and amplified by changing the current density and can thus be useful for spintronics. As a demonstration, we show how the proposal can be employed as electrically reconfigurable magnonic diodes and for realizing logic operations. A particular advantage is that a relatively small current density is sufficient for signal control. Particularly, when the magnonic bands approach each other, the required current density needed to approach the *PT*-symmetry phase transition decreases. The band dispersion can be modulated and gaped by using a periodic *PT*-symmetric structure. In addition to potential use in magnonic devices, the proposed magnonic *PT*-symmetric crystal can serve to demonstrate the interplay between

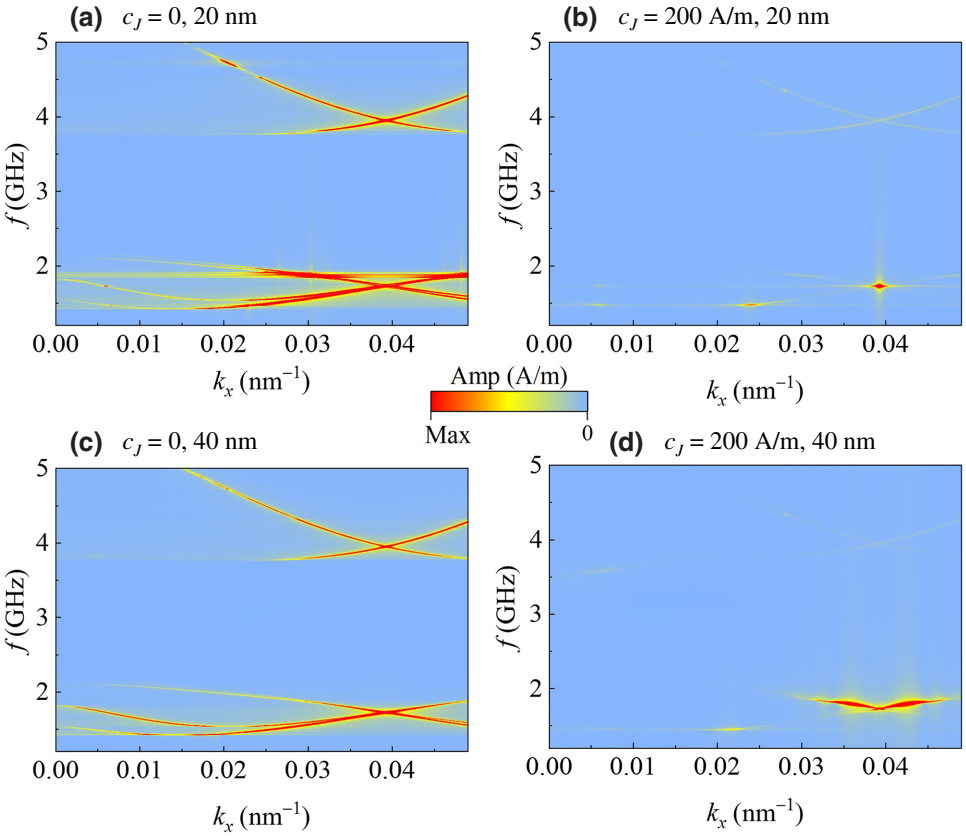

FIG. 8. Shifting the WG1 along x direction by the distance (a),(b) 20 nm or (c),(d) 40 nm, simulated SW dispersion relation of the coupled waveguides for $c_J = 0$ and $c_J = 200$ A/m.

symmetry, damping, and nonlinear effects on the band structure of waves scattered from a periodic potential.

ACKNOWLEDGMENTS

This work is supported by the DFG through SFB TRR227, and Project No. 465098690, the National Natural Science Foundation of China (Grants No. 12174452, No. 12074437, No. 11704415, No. 11674400, and No. 52073308), and the Natural Science Foundation of Hunan Province of China (Grants No. 2022JJ20050, No. 2021JJ30784, and No. 2020JJ4104).

[1] A. V. Chumak, V. I. Vasyuchka, A. A. Serga, and B. Hillebrands, Magnon spintronics, Nat. Phys. **11**, 453 (2015).
[2] V. V. Kruglyak, S. O. Demokritov, and D. Grundler, Magnonics, J. Phys. D: Appl. Phys. **43**, 264001 (2010).
[3] A. A. Serga, A. V. Chumak, and B. Hillebrands, YIG magnonics, J. Phys. D: Appl. Phys. **43**, 264002 (2010).
[4] J. Lan, W. Yu, R. Wu, and J. Xiao, Spin-Wave Diode, Phys. Rev. X **5**, 041049 (2015).
[5] A. Mahmoud, F. Ciubotaru, F. Vanderveken, A. V. Chumak, S. Hamdioui, C. Adelmann, and S. Cotofana, Introduction to spin wave computing, J. Appl. Phys. **128**, 161101 (2020).
[6] X.-g. Wang, L. Chotorlishvili, G.-h. Guo, and J. Berakdar, Electric field controlled spin waveguide phase shifter in YIG, J. Appl. Phys. **124**, 073903 (2018).
[7] A. Khitun, M. Bao, and K. L. Wang, Magnonic logic circuits, J. Phys. D: Appl. Phys. **43**, 264005 (2010).
[8] K. Vogt, F. Y. Fradin, J. E. Pearson, T. Sebastian, S. D. Bader, B. Hillebrands, A. Hoffmann, and H. Schultheiss, Realization of a spin-wave multiplexer, Nat. Commun. **5**, 3727 (2014).
[9] K.-S. Lee and S.-K. Kim, Conceptual design of spin wave logic gates based on a Mach–Zehnder-type spin wave interferometer for universal logic functions, J. Appl. Phys. **104**, 053909 (2008).
[10] A. V. Chumak, A. A. Serga, and B. Hillebrands, Magnon transistor for all-magnon data processing, Nat. Commun. **5**, 4700 (2014).
[11] M. Balynsky, D. Gutierrez, H. Chiang, A. Kozhevnikov, G. Dudko, Y. Filimonov, A. A. Balandin, and A. Khitun, A magnetometer based on a spin wave interferometer, Sci. Rep. **7**, 11539 (2017).
[12] Q. Wang, P. Pirro, R. Verba, A. Slavin, B. Hillebrands, and A. V. Chumak, Reconfigurable nanoscale spin-wave directional coupler, Sci. Adv. **4**, e1701517 (2018).
[13] A. V. Sadovnikov, E. N. Beginin, S. E. Sheshukova, D. V. Romanenko, Y. P. Sharaevskii, and S. A. Nikitov, Directional multimode coupler for planar magnonics: Side-coupled magnetic stripes, Appl. Phys. Lett. **107**, 202405 (2015).
[14] Q. Wang, M. Kewenig, M. Schneider, R. Verba, F. Kohl, B. Heinz, M. Geilen, M. Mohseni, B. Lägel, F. Ciubotaru, C. Adelmann, C. Dubs, S. D. Cotofana, O. V. Dobrovolskiy, T. Brächer, P. Pirro, and A. V. Chumak, A magnonic directional coupler for integrated magnonic half-adders, Nat. Electron. **3**, 765 (2020).
[15] A. V. Sadovnikov, A. A. Grachev, V. A. Gubanov, S. A. Odintsov, A. A. Martyshkin, S. E. Sheshukova, Y. P. Sharaevskii, and S. A. Nikitov, Spin-wave intermodal coupling in the interconnection of magnonic units, Appl. Phys. Lett. **112**, 142402 (2018).
[16] Z. Ren, S. Liu, L. Jin, T. Wen, Y. Liao, X. Tang, H. Zhang, and Z. Zhong, Reconfigurable nanoscale spin-wave directional coupler using spin-orbit torque, Sci. Rep. **9**, 7093 (2019).
[17] A. V. Sadovnikov, A. A. Grachev, E. N. Beginin, S. E. Sheshukova, Y. P. Sharaevskii, and S. A. Nikitov, Voltage-Controlled Spin-Wave Coupling in Adjacent Ferromagnetic-Ferroelectric Heterostructures, Phys. Rev. Appl. **7**, 014013 (2017).
[18] Y. Fan, P. Quarterman, J. Finley, J. Han, P. Zhang, J. T. Hou, M. D. Stiles, A. J. Grutter, and L. Liu, Manipulation of Coupling and Magnon Transport in Magnetic Metal-Insulator Hybrid Structures, Phys. Rev. Appl. **13**, 061002 (2020).
[19] X.-g. Wang, L. Chotorlishvili, G.-h. Guo, and J. Berakdar, High-Fidelity Magnonic Gates for Surface Spin Waves, Phys. Rev. Appl. **12**, 034015 (2019).
[20] C. M. Bender and S. Boettcher, Real Spectra in Non-Hermitian Hamiltonians Having $\mathcal{PT}$ Symmetry, Phys. Rev. Lett. **80**, 5243 (1998).
[21] C. M. Bender, D. C. Brody, and H. F. Jones, Complex Extension of Quantum Mechanics, Phys. Rev. Lett. **89**, 270401 (2002).
[22] C. M. Bender, Making sense of non-Hermitian Hamiltonians, Rep. Prog. Phys. **70**, 947 (2007).
[23] L. Feng, Z. J. Wong, R.-M. Ma, Y. Wang, and X. Zhang, Single-mode laser by parity-time symmetry breaking, Science **346**, 972 (2014).
[24] R. El-Ganainy, K. G. Makris, M. Khajavikhan, Z. H. Musslimani, S. Rotter, and D. N. Christodoulides, Non-Hermitian physics and PT symmetry, Nat. Phys. **14**, 11 (2018).
[25] C. E. Rüter, K. G. Makris, R. El-Ganainy, D. N. Christodoulides, M. Segev, and D. Kip, Observation of parity-time symmetry in optics, Nat. Phys. **6**, 192 (2010).
[26] A. Regensburger, C. Bersch, M.-A. Miri, G. Onishchukov, D. N. Christodoulides, and U. Peschel, Parity-time synthetic photonic lattices, Nature **488**, 167 (2012).
[27] M.-A. Miri and A. Alù, Exceptional points in optics and photonics, Science **363**, eaar7709 (2019).
[28] X. Zhu, H. Ramezani, C. Shi, J. Zhu, and X. Zhang, $\mathcal{PT}$-Symmetric Acoustics, Phys. Rev. X **4**, 031042 (2014).
[29] R. Fleury, D. Sounas, and A. Alù, An invisible acoustic sensor based on parity-time symmetry, Nat. Commun. **6**, 5905 (2015).
[30] S. Assawaworrarit, X. Yu, and S. Fan, Robust wireless power transfer using a nonlinear parity-time-symmetric circuit, Nature **546**, 387 (2017).
[31] P.-Y. Chen, M. Sakhdari, M. Hajizadegan, Q. Cui, M. M.-C. Cheng, R. El-Ganainy, and A. Alù, Generalized parity-time symmetry condition for enhanced sensor telemetry, Nat. Electron. **1**, 297 (2018).
[32] J. M. Lee, T. Kottos, and B. Shapiro, Macroscopic magnetic structures with balanced gain and loss, Phys. Rev. B **91**, 094416 (2015).

[33] D. Zhang, X.-Q. Luo, Y.-P. Wang, T.-F. Li, and J. Q. You, Observation of the exceptional point in cavity magnon-polaritons, Nat. Commun. **8**, 1368 (2017).

[34] H. Yang, C. Wang, T. Yu, Y. Cao, and P. Yan, Antiferromagnetism Emerging in a Ferromagnet with Gain, Phys. Rev. Lett. **121**, 197201 (2018).

[35] A. Galda and V. M. Vinokur, Exceptional points in classical spin dynamics, Sci. Rep. **9**, 17484 (2019).

[36] H. Liu, D. Sun, C. Zhang, M. Groesbeck, R. Mclaughlin, and Z. V. Vardeny, Observation of exceptional points in magnonic parity-time symmetry devices, Sci. Adv. **5**, eaax9144 (2019).

[37] X.-g. Wang, G.-h. Guo, and J. Berakdar, Steering magnonic dynamics and permeability at exceptional points in a parity–time symmetric waveguide, Nat. Commun. **11**, 5663 (2020).

[38] X.-g. Wang, G.-h. Guo, and J. Berakdar, Enhanced Sensitivity at Magnetic High-Order Exceptional Points and Topological Energy Transfer in Magnonic Planar Waveguides, Phys. Rev. Appl. **15**, 034050 (2021).

[39] X.-G. Wang, G.-H. Guo, and J. Berakdar, Electric steering of spin excitation in nanostructured synthetic antiferromagnet, Appl. Phys. Lett. **117**, 242406 (2020).

[40] C.-W. Sui, S.-H. Yuan, X.-G. Wang, J. Berakdar, and C. Jia, Emergent magnonic singularities in anti parity-time symmetric synthetic antiferromagnets, New J. Phys. **24**, 023031 (2022).

[41] H. Hodaei, A. U. Hassan, S. Wittek, H. Garcia-Gracia, R. El-Ganainy, D. N. Christodoulides, and M. Khajavikhan, Enhanced sensitivity at higher-order exceptional points, Nature **548**, 187 (2017).

[42] J. Wiersig, Prospects and fundamental limits in exceptional point-based sensing, Nat. Commun. **11**, 2454 (2020).

[43] J. Zhang, B. Peng, Ş. K. Özdemir, K. Pichler, D. O. Krimer, G. Zhao, F. Nori, Y.-x. Liu, S. Rotter, and L. Yang, A phonon laser operating at an exceptional point, Nat. Photonics **12**, 479 (2018).

[44] Y.-H. Lai, Y.-K. Lu, M.-G. Suh, Z. Yuan, and K. Vahala, Observation of the exceptional-point-enhanced Sagnac effect, Nature **576**, 65 (2019).

[45] J. Wiersig, Enhancing the Sensitivity of Frequency and Energy Splitting Detection by using Exceptional Points: Application to Microcavity Sensors for Single-Particle Detection, Phys. Rev. Lett. **112**, 203901 (2014).

[46] T. Yu, H. Yang, L. Song, P. Yan, and Y. Cao, Higher-order exceptional points in ferromagnetic trilayers, Phys. Rev. B **101**, 144414 (2020).

[47] M. Krawczyk and D. Grundler, Review and prospects of magnonic crystals and devices with reprogrammable band structure, J. Phys.: Condens. Matter **26**, 123202 (2014).

[48] A. V. Chumak, A. A. Serga, and B. Hillebrands, Magnonic crystals for data processing, J. Phys. D: Appl. Phys. **50**, 244001 (2017).

[49] I. N. Krivorotov, N. C. Emley, J. C. Sankey, S. I. Kiselev, D. C. Ralph, and R. A. Buhrman, Time-domain measurements of nanomagnet dynamics driven by spin-transfer torques, Science **307**, 228 (2005).

[50] M. Collet, X. de Milly, O. d'Allivy Kelly, V. V. Naletov, R. Bernard, P. Bortolotti, J. Ben Youssef, V. E. Demidov, S. O. Demokritov, J. L. Prieto, M. Muñoz, V. Cros, A. Anane, G. de Loubens, and O. Klein, Generation of coherent spin-wave modes in yttrium iron garnet microdiscs by spin-orbit torque, Nat. Commun. **7**, 10377 (2016).

[51] R. Verba, V. Tiberkevich, K. Guslienko, G. Melkov, and A. Slavin, Theory of ground-state switching in an array of magnetic nanodots by application of a short external magnetic field pulse, Phys. Rev. B **87**, 134419 (2013).

[52] A. Haldar, D. Kumar, and A. O. Adeyeye, A reconfigurable waveguide for energy-efficient transmission and local manipulation of information in a nanomagnetic device, Nat. Nanotech. **11**, 437 (2016).

[53] R. Verba, G. Melkov, V. Tiberkevich, and A. Slavin, Collective spin-wave excitations in a two-dimensional array of coupled magnetic nanodots, Phys. Rev. B **85**, 014427 (2012).

[54] A. Mostafazadeh, Exact *PT*-symmetry is equivalent to Hermiticity, J. Phys. A: Math. Gen. **36**, 7081 (2003).

[55] See Supplemental Material at http://link.aps.org/supplemental/10.1103/PhysRevApplied.18.024080 for the calculations and analytical derivation of four coupled waveguides.

[56] Y. A. Vlasov, M. O'Boyle, H. F. Hamann, and S. J. McNab, Active control of slow light on a chip with photonic crystal waveguides, Nature **438**, 65 (2005).

[57] Y. Akahane, T. Asano, B.-S. Song, and S. Noda, High-Q photonic nanocavity in a two-dimensional photonic crystal, Nature **425**, 944 (2003).

[58] V. V. Konotop and B. I. Mantsyzov, Light propagation through a PT-symmetric photonic-crystal, Opt. Express **24**, 26146 (2016).

[59] A. Ramasubramaniam, D. Naveh, and E. Towe, Tunable band gaps in bilayer transition-metal dichalcogenides, Phys. Rev. B **84**, 205325 (2011).

[60] Y. Chen, J. Xi, D. O. Dumcenco, Z. Liu, K. Suenaga, D. Wang, Z. Shuai, Y.-S. Huang, and L. Xie, Tunable band gap photoluminescence from atomically thin transition-metal dichalcogenide alloys, ACS Nano **7**, 4610 (2013).

[61] C. Pan, C.-Y. Wang, S.-J. Liang, Y. Wang, T. Cao, P. Wang, C. Wang, S. Wang, B. Cheng, A. Gao, E. Liu, K. Watanabe, T. Taniguchi, and F. Miao, Reconfigurable logic and neuromorphic circuits based on electrically tunable two-dimensional homojunctions, Nat. Electron. **3**, 383 (2020).

[62] J. Topp, D. Heitmann, M. P. Kostylev, and D. Grundler, Making a Reconfigurable Artificial Crystal by Ordering Bistable Magnetic Nanowires, Phys. Rev. Lett. **104**, 207205 (2010).

[63] Q. Wang, A. V. Chumak, L. Jin, H. Zhang, B. Hillebrands, and Z. Zhong, Voltage-controlled nanoscale reconfigurable magnonic crystal, Phys. Rev. B **95**, 134433 (2017).

[64] E. R. Lewis, D. Petit, L. O'Brien, A. Fernandez-Pacheco, J. Sampaio, A.-V. Jausovec, H. T. Zeng, D. E. Read, and R. P. Cowburn, Fast domain wall motion in magnetic comb structures, Nat. Mater. **9**, 980 (2010).

[65] V. S. Tkachenko, A. N. Kuchko, M. Dvornik, and V. V. Kruglyak, Propagation and scattering of spin waves in curved magnonic waveguides, Appl. Phys. Lett. **101**, 152402 (2012).

[66] K.-S. Lee, D.-S. Han, and S.-K. Kim, Physical Origin and Generic Control of Magnonic Band Gaps of Dipole-Exchange Spin Waves in Width-Modulated Nanostrip Waveguides, Phys. Rev. Lett. **102**, 127202 (2009).

[67] K. Di, H. S. Lim, V. L. Zhang, S. C. Ng, M. H. Kuok, H. T. Nguyen, and M. G. Cottam, Tuning the band structures of a one-dimensional width-modulated magnonic crystal by a transverse magnetic field, J. Appl. Phys. **115**, 053904 (2014).

[68] G. Gubbiotti, L. L. Xiong, F. Montoncello, L. Giovannini, and A. O. Adeyeye, Spin wave dispersion and intensity correlation in width-modulated nanowire arrays: A Brillouin light scattering study, J. Appl. Phys. **124**, 083903 (2018).

[69] S.-K. Kim, K.-S. Lee, and D.-S. Han, A gigahertz-range spin-wave filter composed of width-modulated nanostrip magnonic-crystal waveguides, Appl. Phys. Lett. **95**, 082507 (2009).